Cloud Detection Methodology Based on a Sky-imaging System

5 authors, including:

Rémi Chauvin
French National Centre for Scientific Research
15 PUBLICATIONS   **31** CITATIONS

Stéphane Grieu
Université de Perpignan
90 PUBLICATIONS   **493** CITATIONS

Some of the authors of this publication are also working on these related projects:

Solar resource assessment and forecasting View project

International Conference on Concentrating Solar Power and Chemical Energy Systems,
SolarPACES 2014

Cloud detection methodology based on a sky-imaging system

R. Chauvin[1], J. Nou[1], S. Thil[1,2], A. Traoré[1,2] and S. Grieu[1,2,*]

[1]*PROMES-CNRS, Rambla de la thermodynamique, Tecnosud, 66100 Perpignan, France*
[2]*University of Perpignan Via Domitia, 52 Avenue Paul Alduy, 66860 Perpignan, France*

Abstract

This paper deals with an image processing methodology based on a sky-imaging system developed at the PROMES-CNRS laboratory. It is a part of a project which aims at improving solar plant control procedures using Direct Normal Irradiance (DNI) forecasts under various sky conditions at short term horizon (5-30 minutes) and high spatial resolution (~1 km²). The work presented in this paper is about the improvement of the cloud cover estimation, which is the main step in DNI forecasting. First, an overview of the existing sky-imaging systems and the current cloud detection algorithms is presented. Next, the experimental setup is introduced. Then, the methodology used to estimate the cloud cover is detailed. Finally, the paper ends with some results and discussion.

Keywords: Sky-imaging system; cloud cover; clear-sky irradiance; thresholding techniques.

1. Introduction

It is widely acknowledged by solar companies and plant operators that cost remains the main drawback of Concentrating Solar Power (CSP) systems. In that context, the CSPIMP (Concentrated Solar Power efficiency IMProvement) project has been initiated in 2013 in order to make CSP plants more competitive. The main target of the project is to improve plant efficiency by developing better procedures for steam turbine start up cycles, maintenance activities and plant control. Regarding the plant control procedures, solar resource assessment and forecasting allow the plant operators to better manage the solar field and the heat transfer fluid flow in real-time.

* Corresponding author. Tel.: +33468682257; Fax: +33468682213.
  E-mail address: stephane.grieu@promes.cnrs.fr

Depending on the CSP configuration (turbine, back-up generator, buffer tank, storage system…), a customized forecasting model must be built to deal with the plant's behavior against solar variability. At very short-term (5-30 minutes) and high spatial resolution (~ 100 m²), models based on sky-imaging systems are the most suitable for solar resource forecasting [1–3]. Indeed, these systems provide a hemispherical view of the whole sky, allowing the cloud cover and the cloud motion to be measured. Both are essential in order to forecast the direct beam attenuation produced by clouds. In that context, we decided to focus our work on this approach because short-term forecasting is a key step to improve solar power plants management. Indeed, a sky-imaging system can help the power plant owner to reduce its fees by taking advantage of the solar variability forecast and improve the control procedure in real-time.

Among the existing commercial sky-imaging systems, the most known is the *Total Sky Imager* developed by Yankee Environmental Systems. It uses a hemispherical mirror to reflect the sky hemisphere into a downward-pointing camera. Other industrial sky imagers exist, such as the *SRF-02* and the *VISJ1006* cameras, respectively developed by EKO Instruments and Schreder CMS. However, these commercial solutions suffer from a low camera resolution and limited possibilities of customization, preventing any improvement specific to the power plant needs. On the other hand, many customized solutions have been used for research applications, using a non commercial sky imager. One of the first major systems is the *Whole Sky Imager* developed since the 1980s [4] for military applications by the Atmospheric Radiation Measurement Climate Research Facility. The system is able to detect clouds during daytime and nighttime thanks to very sophisticated algorithms with accurate detection of haze, thin clouds and opaque clouds. Nevertheless, it is not inexpensive to build a system with such qualities. As a consequence, other laboratories have developed cost-effective alternative systems based on a camera equipped with a fisheye lens and protected by a weatherproof enclosure [5, 6]. Among them, we find the *Whole Sky Camera*, developed by the University of Girona [7], the *All-Sky Imager* developed at the University of Granada [8] or the sky imager developed by the University of California, San Diego (UCSD) [3]. The *UCSD Sky Imager* (USI) seems to be the most advanced system. It is specifically designed for the short-term forecasting of solar irradiance. It involves high quality components associated with sophisticated algorithms. The USI is able to provide a cloud map of the studied location, allowing the forecast of ramp events for large solar plants. However, according to their authors, a large part of improvement is still possible, both in technical and scientific terms [3]. Nevertheless, the first works published by these laboratories are encouraging and motivated PROMES-CNRS to get involved in this challenging topic. Consequently, an experimental unit has been installed on the laboratory roof in 2013 in order to develop a customized forecasting tool.

To predict the solar resource at short notice, the cloud distribution above the camera must be known. The accuracy of this localization strongly influences the overall performance of the forecasting process. As a consequence, the cloud detection algorithm must be as robust as possible for all kinds of sky conditions. Cloud detection consists in classifying pixels either as cloud or sky. Different cloud detection methods already exist. They are generally based on thresholding techniques [9–13], neural networks models [8, 14] or more sophisticated approaches including the Markov Random Fields (MRF) models [15], the Gaussian Mixture Models (GMM) [16] or the normalized cut method [17]. Thresholding techniques are widely used because of their simplicity and the limited amount of computational time needed to perform the pixel identification. On the other hand, neural networks models can achieve results with higher quality but they need a long pre-processing time to get a large set of identified pixels used during the training step. Finally, more sophisticated models, like MRF and GMM, use both pixels information and their spatial distribution to outperform usual techniques, especially for thin cloud detection. However, these models are time-consuming and can hardly be integrated into a real-time process. Since image processing have to be achieved at a high rate in our application (images are collected every 20 seconds), it has been decided to focus on thresholding techniques. However, the classic thresholding methods have to be improved: their results are unsatisfactory, especially when the image has thin clouds, exhibits a strong gradient (e.g. during sunrise or sunset), or in areas near the sun.

This paper introduces a new cloud detection methodology, based on thresholding techniques improved by a background subtraction. It is organized as follows. Section 2 introduces the experimental setup. Section 3 details the cloud detection algorithm. Section 4 presents the results.

2. Experimental setup

PROMES-CNRS decided to build its own system, fully customizable both from a hardware and software point of view. This decision is motivated by the fact that all the existing sky imagers suffer from drawbacks and PROMES-CNRS believes that a custom solution would make such systems more attractive. After a detailed review of the different cameras proposed by manufacturers, a 5 megapixels camera with a color CMOS sensor has been selected. The camera, named 5481VSE-C and provided by IDS-imaging, is equipped with a Fujinon fisheye lens and protected by a waterproof enclosure manufactured by autoVimation (Fig. 1). A CMOS sensor has been preferred to a CCD sensor because in the CCD structure charge flows in the direction where pixels are read, whereas in CMOS sensors the readout is performed locally at each pixel. It results that CMOS sensors are inherently more resilient to smear effect and blooming than CCD sensors near the sun area. Moreover, the camera is simple and easy to setup and operate thanks to its on-board video server offering an intuitive browser-based interface. It is also easy to integrate thanks to the power supplied via Ethernet and the minimal memory requirements because of the MJPEG data compression format. Images are collected every 20 seconds at a resolution of 1920 x 2560 pixels with 8 bits per channel. Finally, the PROMES sky imager is not equipped with a solar occulting device which is frequently used to reduce the light intensity reaching the sensor. Indeed, although this device improves the sky visibility by reducing pixels saturation, it occults the circumsolar area which provides vital information concerning the very short term solar irradiance fluctuations. To sum up, the advantages of our system over standard sky imagers include high quality components, a high sensor resolution, a robust build, a small form factor and a full programmability.
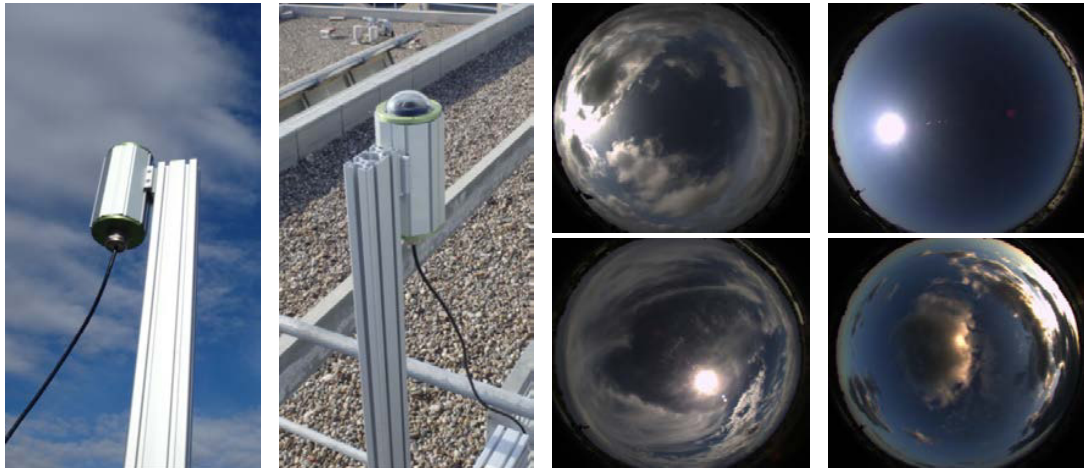

Fig. 1. PROMES-CNRS sky imager and a few snapshots.

3. Cloud detection algorithm

In this section, the cloud detection algorithm is detailed. First, the calibration step, which is essential in the development of our algorithm, is briefly described. Then, the existing features used to exhibit cloud patterns are presented. Next, the clear-sky pixel distribution function is introduced. This function allows clear sky images to be generated from various types of sky images. Finally the pixel identification, based on a thresholding technique applied on the image, corrected by the clear sky image, is described.

3.1. Camera calibration

A geometric angular calibration of the camera has been performed in order to get the relationship between a given pixel on the image and its projection onto the unit sphere. The OcamCalib toolbox [18] has been used to calibrate the camera. It allows an easy calibration of the camera through two steps. First, pictures of a checkerboard

in different positions and orientations are taken (Fig. 2). Then, an automatic corner extraction is performed and a least square linear minimization method is used to fit these points with a four-order polynomial. Once the camera is calibrated, it is possible to calculate the Pixel/Zenith Angle (PZA) and the Pixel/Azimuth Angle (PAA) for every pixel on the image, assuming that the camera is pointing the zenith. However, this last assumption is generally not met: the camera is not perfectly aligned with the zenith in reality. Thus, during operating time, a second calibration is automatically performed daily, using the sun position: since the misalignment with the zenith produces a wrong detection of the sun on the image, the camera orientation can be corrected by comparing the real position of the sun with its position on the image. The real position of the sun is calculated using the SG2 algorithm [19], whereas the position of the sun on the image is computed using the circular Hough transform. Finally, from a set of theoretical and real points acquired through the day, a rotation matrix is computed to correct PZA and PAA. In the end, it is possible to get the sun position on the image at any moment, even during cloudy days (Fig. 2). This calibration also enables the computation of the Sun/Pixel Angle (SPA) for every pixel on the image.
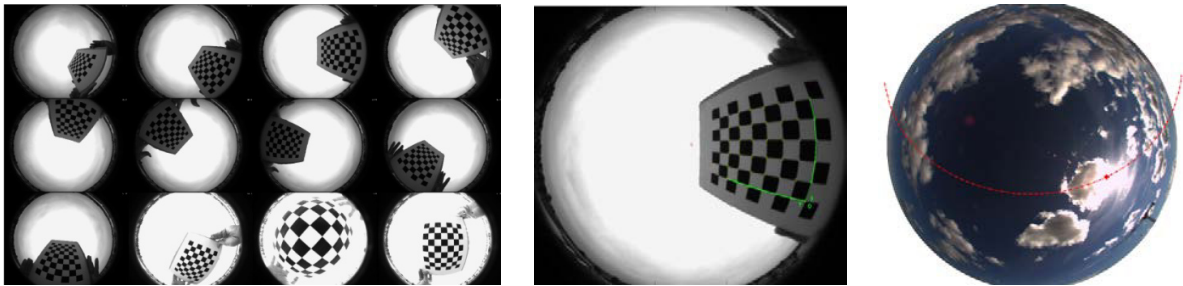

Fig. 2. PROMES sky imager calibration and the resulting sun path.

3.2. Image features

As mentioned before, it has been decided to apply a thresholding technique on sky images in order to perform the pixel identification. However, pixels on sky images can be generally classified more easily with a threshold applied on features adapted to the sky characteristics rather than a threshold directly applied on RGB components of the image. Many features have been suggested to better represent physical, visual or statistical properties of the sky. The following table summarizes the main features commonly used in the cloud detection algorithms:

Table 1. Main features used for cloud pixel identification.

Feature	Equation	Range	References
Red/Blue Difference (RBD)	$RBD = R - B$	[-255,255]	[10]
Red/Blue Ratio (RBR)	$RBR = \dfrac{R}{B}$	[0,255]	[7,20]
Normalized Red/Blue Ratio (NRBR)	$NRBR = \dfrac{R - B}{R + B}$	[-1,1]	[11], [15–17], [21]
Saturation (Sat)	$Sat = 1 - \dfrac{min(R,G,B)}{max(R,G,B)}$	[0,1]	[9,15,16]
Euclidean Geometric Distance (EGD)	$EGD = \sqrt{R^2 + G^2 + B^2 + \dfrac{(R+G+B)^2}{3}}$	[0,208]	[12,15,16]

The three first features, RBD, RBR and NRBR, describe the physical properties of the sky. Indeed, the Rayleigh scattering is inversely proportional to the fourth power of the wavelength; it implies that the visible light in the blue spectrum is predominately scattered in the atmosphere, whereas cloud particles scatter the blue and red light almost equally. It results that clear sky appears blue (high NRBR) and clouds appear white or grey (low NRBR).

The saturation feature represents the intensity distribution across the spectrum. For instance, the most saturated color is obtained by using only one wavelength at a high intensity. As a consequence, clear sky has a high saturation value whereas clouds are generally less colorful and thus have a low saturation value.

Finally, the EGD feature represents the distance between the color vector of a pixel and the diagonal of the RGB cube. It has been noticed that cloud pixels are more evenly distributed along the diagonal of the RGB cube (low EGD) than clear sky pixels which are located farther (high EGD) [12]. To perform the pixel identification, we decided to use the NRBR feature due to its ability to improve the visual contrast between sky and clouds and its robustness to noise [11].

3.3. Generation of clear-sky images

The main problem in pixel identification using thresholding techniques is the non-uniformity of the sky background. Indeed, clear sky pixels appear white in the circumsolar area and near horizon whereas they are bluer in the other parts of the sky. It results that the sun area and the horizon are often incorrectly classified as clouds. To improve the cloud detection algorithm, an idea would then be to remove the spatial dependency of the clear sky pixels from the NRBR feature. According to the CIE Standard Clear Sky model [22], the relative clear sky luminance L can be modelled as a function of PZA and SPA and is given by:

$$L(PZA, SPA) = \left[1 - exp\left(\frac{-0.32}{\cos(PZA)}\right)\right] . [0.91 + 10. exp(-3. SPA) + 0.45. \cos(SPA)^2] \qquad (1)$$

This function has been already used to simulate both the sky luminance and the sky radiance distributions for various sky conditions [23, 24]. A new equation, inspired by these works, has been developed to fit with the clear-sky pixels distribution I_p provided by our sky imager:

$$I_p(PZA, SPA) = a_1 . \left[1 + a_2 . exp\left(\frac{a_3}{\cos(PZA)}\right)\right] . [a_4 + a_5 . SPA^{a_6} + a_7 . \cos(SPA)^2] \qquad (2)$$

This equation gives the expected value of the sky background as a function of PZA and SPA. In comparison to (1), the main modification is in the "pixel intensity profile" in the circumsolar area (low SPA). Indeed, as suggested by the CIE, this profile exhibits near the sun an exponential dependence (i.e. $a_5 . \exp(a_6 . SPA)$), whereas (2) has a linear relationship in log-log space in this region (i.e. $a_5 . SPA^{a_6}$). This modification has been motivated by visual observation of the intensity profile in the sun area. Furthermore, the linear relationship in log-log space, at low SPA, is more consistent with the sunshape profile described by Buie [25].

The seven coefficients $(a_i)_{1 \leq i \leq 7}$ used to fit the sky images are determined by a regression analysis using a least square error minimization method. The fitting process is detailed in Section 4. It has been observed that these coefficients are related to some atmospheric properties, like the optical depth and the air mass, and so would be useful information for the plant operator. More details concerning equation (2) and its coefficients will soon be available as a separate publication. Once the coefficients are estimated, it is possible to generate a clear sky image from any image took by the sky imager. Fig. 3 illustrates the clear sky image generated using equation (2) and an image taken with the PROMES sky imager:
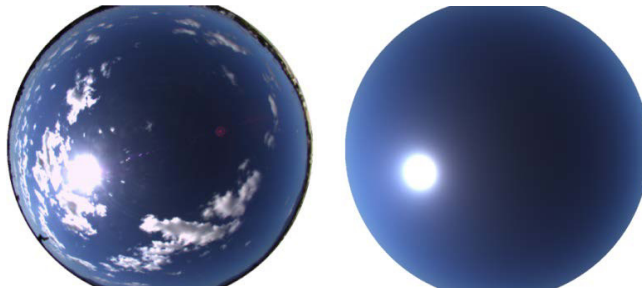

Fig. 3. An image took with the sky imager and the generated clear sky image.

3.4. Cloud detection method

As seen before, pixel identification is mainly based on thresholding techniques applied on a feature well adapted to cloud detection. The most classical algorithms use a fixed threshold where pixels whose NRBR is less than the threshold are classified as clear sky pixels [7]. These algorithms often use different fixed thresholds as a function of the SPA in order to reduce the number of misclassified pixels due to the non-uniformity of the sky background. The main drawback of this local thresholding method is that the thresholds depend on the camera and climate characteristics. For instance, two cameras located at the same place or one camera installed at different locations may have different fixed thresholds. Moreover, the fixed threshold does not integrate the atmospheric turbidity fluctuations. Indeed, in a clean and cloudless atmosphere, Rayleigh scattering dominates, whereas in a very turbid atmosphere, incoming solar radiation is scattered due to both Mie and Rayleigh scattering. Since Mie scattering is less dependent on wavelength, the sky is less blue during polluted days. It results that clear sky pixels can be wrongly classified when turbidity is high.

Pixel identification can also be performed using an adaptive thresholding method based on the Otsu algorithm [26]. In this method, the threshold is calculated from the NRBR histogram, assuming that the image only contains two classes of pixels (cloud and clear sky pixels). The optimal threshold is found by minimizing the intra-class variance of those two classes. Although this technique is more robust against turbidity fluctuations and for thin cloud detection, it produces significant errors during fully overcast or clear sky days, as the NRBR histogram is unimodal in such cases. As a consequence, hybrid algorithms have been developed to combine the advantages of fixed and adaptive thresholding techniques [11]. Basically, the sky images are divided into two groups which are unimodal and bimodal images. Pixels of unimodal images are classified using the fixed thresholding method whereas pixels of bimodal images are classified using an adaptive threshold.

Thresholding techniques have difficulties to deal with the spatial and temporal non-uniformity of the sky background. The idea is then to use generated clear-sky images to simplify the cloud detection algorithm: the thresholding is not applied on the current image's NRBR, but on the NRBR difference between the current image and its corresponding clear sky image. This has many advantages:

- The use of local thresholding methodologies is avoided by removing the clear-sky non-uniformity from images,
- The threshold is much less dependent on the camera and climate characteristics, since the camera and climate characteristics are mostly removed during the subtraction process,
- The temporal fluctuations of the threshold are also removed, since the clear sky image also integrates atmospheric turbidity effects.

The thresholding process is done in two steps. First, the NRBR of the current image and its corresponding clear sky image are generated (named respectively NRBR and $NRBR_{cs}$). Then the difference between these two NRBR images is calculated:

$$\Delta_{NRBR} = |NRBR - NRBR_{cs}| \qquad (3)$$

Pixels for which Δ_{NRBR} is above 0.15 are classified as cloud pixels.

4. Results and discussion

This part provides some details about the clear sky image generation process and the cloud detection algorithm. First, the fitting algorithm is described. Then the ability of the fitting algorithm to accurately generate clear sky images is tested. Finally, an evaluation of the cloud detection algorithm is presented.

4.1. Fitting algorithm

As seen before, the equation is fitted on sky images using a set of seven coefficients. However, this time-consuming process must be achieved faster than the elapsed time between two snapshots (i.e. 20 seconds). Two options have been considered to reduce the computation time of the fitting algorithm. The first one concerns the

definition of the bounds and the starting values of the seven coefficients. After a few preliminary studies, it has been decided to set the bounds and starting values as follows:

Table 2. Initial conditions of the seven coefficients.

Coefficient	a_1	a_2	a_3	a_4	a_5	a_6	a_7
Lower bound	0	-2	-2	0.5	0	-5	0
Starting value	100	-1	-0.4	1	200	-3	0.5
Upper bound	200	0	0	1.5	400	-2	2

Note that in a real-time process, the starting values of these seven coefficients can be set to their values calculated during the previous step. Another way to reduce the computation time is to separate the fitting problem in two simpler problems. Indeed, the pixel intensity distribution can be split into:

$$I_p(PZA, SPA) = f_1(PZA).f_2(SPA) \tag{4}$$

where:

$$f_1(PZA) = a_1.\left[1 + a_2.exp\left(\frac{a_3}{\cos(PZA)}\right)\right] \tag{5}$$

is called the gradation function, and:

$$f_2(SPA) = [a_4 + a_5.SPA^{a_6} + a_7.\cos(SPA)^2] \tag{6}$$

is called the scattering function. Table 2 gives the starting values of the seven coefficients. It can be noticed that for SPA close to 90°, the scattering function is close to 1 ($f_2(90°) \approx 1$). Therefore the pixel intensity distribution in this region can be approximated by:

$$I_p(PZA, 90°) \approx f_1(PZA) \tag{7}$$

Consequently, it is possible to evaluate the coefficients a_1, a_2 and a_3 for SPA close to 90°. Fig. 4 shows the determination process of these three coefficients. The red band on the sky image represents the region where pixels have a SPA between 88° and 92°. Clouds are eliminated from this band by removing pixels which have a high NRBR (i.e. $NRBR > -0.2$). The average pixel intensity in this band is then fitted as a function of PZA. In this example (Fig. 4), the fit is performed for PZA going from 45° to 85° with a coefficient of determination R^2 close to 0.99.
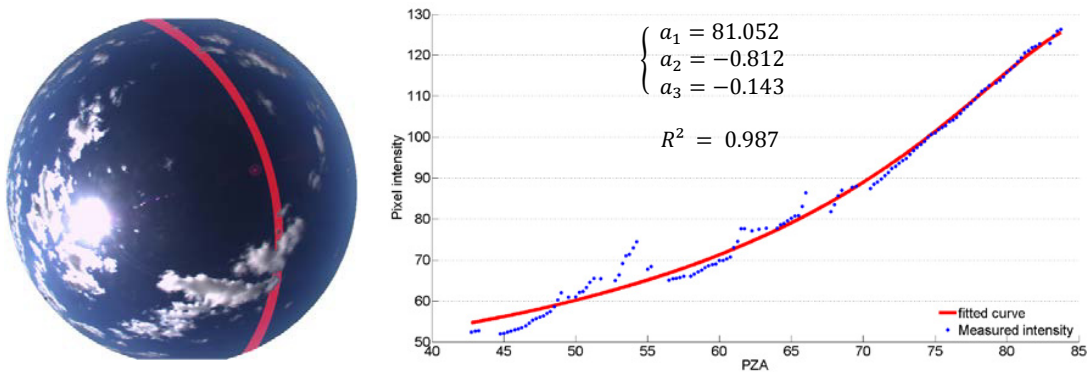

Fig. 4. Evaluation of the coefficients a_1, a_2 and a_3 for the red channel.

Once the coefficients of the gradation function have been evaluated for each color channel (i.e. red, green and blue), the scattering function can be obtained as follows:

$$f_2(SPA) = \frac{I_p(PZA, SPA)}{f_1(PZA)} \tag{8}$$

Fig. 5 shows the determination process of the four coefficients of the scattering function. The green area on the sky image is the region where pixels have been averaged as a function of SPA. One more time, clouds are eliminated from the image by removing pixels having a high NRBR: the sun and the circumsolar area are thus also removed. We can notice that the coefficient of determination is very close to 1. This very good result validates the modification performed on equation (2) about the linear relationship, in log-log space, of the pixel intensity as a function of SPA near the sun.
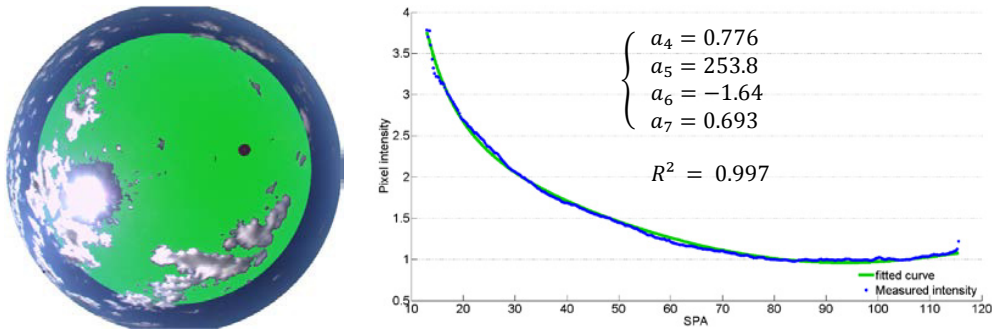

Fig. 5. Evaluation of the coefficients a_4, a_5, a_6 and a_7 for the red channel.

Once the seven coefficients are found for each color channel, it is possible to generate a clear sky image (Fig. 3). Using the proposed approach, it takes approximately 3 seconds to generate a clear sky image from an original image.

4.2. Performance analysis of the clear sky image generation

In order to evaluate the accuracy of equation (2), we compare a set of full clear sky images with their corresponding generated clear sky images. We use the Mean Absolute Error (MAE) and the Root Mean Square Error (RMSE) as evaluation criteria:

$$MAE = \frac{\sum |I_{measured} - I_{estimated}|}{N} \qquad RMSE = \sqrt{\frac{\sum (I_{measured} - I_{estimated})^2}{N}} \tag{9}$$

The errors between the original clear sky image and the generated clear sky image have been computed during a full clear sky days from 10 am to 8 pm, which represents 1890 images. In reality, the day was not fully clear due to some cirrus appearing near the sun after 4 pm. As seen on Fig. 6, from 10 am to 4 pm, we observe that MAE remains below 3% and RMSE below 5%. After 4 pm, MAE increases up to 5% and RMSE up to 10%. It is also noticed that the errors are weakly dependent on solar elevation (i.e. time of the day).
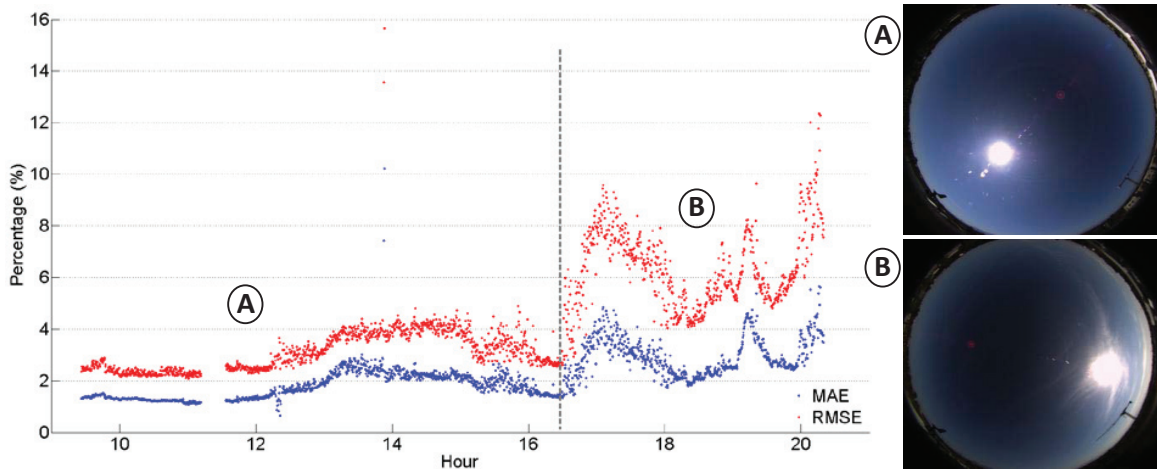
Fig. 6. Evaluation of the pixel intensity distribution function during a full clear sky day.

In addition to the approximation made by the fitting algorithm and the model itself, the error between those images can be explained by camera noise (dark current, readout noise, ...) and artifacts on the actual image (dome soiling, lens flare and blooming effects). However, their respective contributions are difficult to evaluate. Because the RMSE is twice higher than the MAE, we can expect that some outlier values are present. These outlier values are mostly related to the artifacts and soiling which are precisely located on the image, unlike the other sources of errors. Consequently, we can infer that the approximation made by equation (2) does not produce many errors and depicts the clear sky distribution accurately.

4.3. Cloud detection using corrected NRBR

As mentioned before, the NRBR from the generated clear sky image is computed and subtracted from the original NRBR. The subtraction allows the sky non-uniformity to be removed and enables the sun to be differentiated from the clouds (Fig. 7).
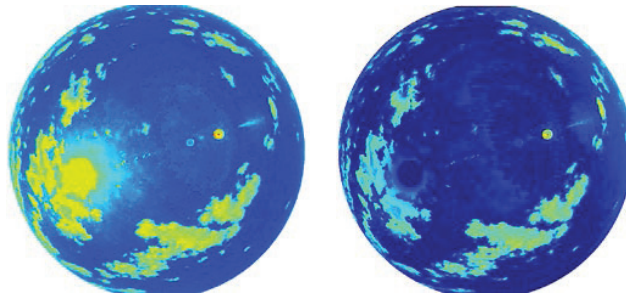

Fig. 7. NRBR of the original image (left) vs. the NRBR corrected by the clear sky image (right).

It is now possible to apply a fixed threshold on the image without any problems of background non-uniformity. We compare our model with a fixed and an adaptive threshold applied on the original NRBR feature. The results are shown in Fig. 8. The fixed threshold was set to -0.1 because it was found to be the best compromise after several tries on test images. The threshold, using the adaptive technique based on the Otsu's method, is estimated to -0.225. It produces a difference of 9.4% between the two techniques, showing that the threshold is highly dependent on the image. Finally, as seen on Fig. 8, the sun is detected as a cloud in both techniques whereas it is correctly detected using our model. Moreover, this algorithm is also able to differentiate clouds from the sun even in the circumsolar area. The difference between the cloud map based on the adaptive threshold and the one using our algorithm is about

6%. Most of the misclassified pixels are located in the circumsolar area. The other parts of the sky are similarly detected.
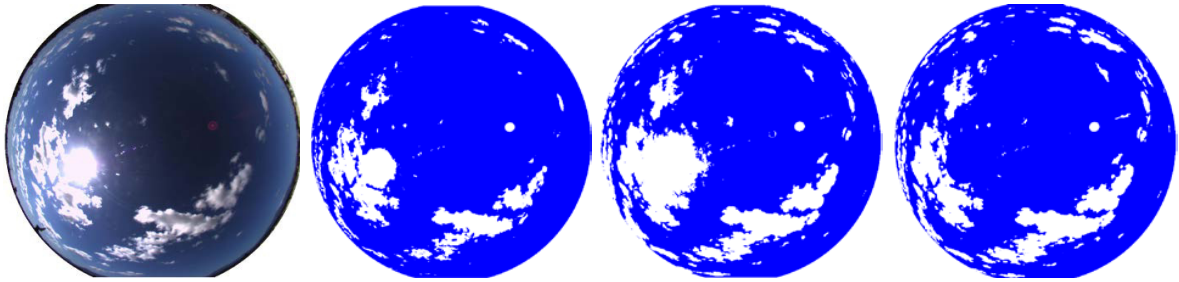

Fig. 8. Cloud map using a fixed and an adaptive thresholding technique in comparison to the cloud map obtained using our model.

5. Conclusion and future work

The main contribution of this work is the development of an algorithm able to generate real-time clear sky images from original images. It allows the background non-uniformity of the sky to be removed. Consequently, the cloud detection algorithm outperforms the standard thresholding techniques, especially in the circumsolar area. It results that the cloud cover is more accurately calculated (about 5%) and the sun area is not systematically detected as a cloud. A better assessment of the cloud cover in real-time would help the CSP plant operator to optimize the use of the solar field and so the overall output of the plant. The next step of this work is to improve the real-time generation of the clear sky images. First, correlations between the seven coefficients and some properties of the atmosphere have to be highlighted. Then, these correlations would help to optimize the initialization of the fitting algorithm.

References

[1] Chow CW, Urquhart B, Lave M, Dominguez A, Kleissl J, Shields J, et al. Intra-hour forecasting with a total sky imager at the UC San Diego solar energy testbed. Solar Energy 2011;85:2881–93. doi:10.1016/j.solener.2011.08.025.
[2] Marquez R, Coimbra CFM. Intra-hour DNI forecasting based on cloud tracking image analysis. Solar Energy 2013;91:327–36. doi:10.1016/j.solener.2012.09.018.
[3] Yang H, Kurtz B, Nguyen D, Urquhart B, Chow CW, Ghonima M, et al. Solar irradiance forecasting using a ground-based sky imager developed at UC San Diego. Solar Energy 2014;103:502–24. doi:10.1016/j.solener.2014.02.044.
[4] Shields JE, Karr ME, Johnson RW, Burden AR. Day/night whole sky imagers for 24-h cloud and sky assessment: history and overview. Applied Optics 2013;52:1605–16.
[5] Pfister G, McKenzie RL, Liley JB, Thomas A, Forgan BW, Long CN. Cloud Coverage Based on All-Sky Imaging and Its Impact on Surface Solar Irradiance. Journal of Applied Meteorology n.d.;42:1421–34.
[6] Marquez R, Coimbra CFM. Forecasting of global and direct solar irradiance using stochastic learning methods, ground experiments and the NWS database. Solar Energy 2011;85:746–56. doi:10.1016/j.solener.2011.01.007.
[7] Long CN, Sabburg JM, Calbó J, Pagès D. Retrieving Cloud Characteristics from Ground-Based Daytime Color All-Sky Images. Journal of Atmospheric and Oceanic Technology 2006;23:633–52. doi:10.1175/JTECH1875.1.
[8] Cazorla Cabrera A. Development of a sky imager for cloud classification and aerosol characterization. Universidad de Granada, 2010.
[9] Souza-Echer MP, Pereira EB, Bins LS, Andrade MAR. A Simple Method for the Assessment of the Cloud Cover State in High-Latitude Regions by a Ground-Based Digital Camera. Journal of Atmospheric and Oceanic Technology 2006;23:437–47. doi:10.1175/JTECH1833.1.
[10] Heinle A, Macke A, Srivastav A. Automatic cloud classification of whole sky images. Atmospheric Measurement Techniques 2010;3:557–67. doi:10.5194/amt-3-557-2010.
[11] Li Q, Lu W, Yang J. A Hybrid Thresholding Algorithm for Cloud Detection on Ground-Based Color Images. Journal of Atmospheric and Oceanic Technology 2011;28:1286–96. doi:10.1175/JTECH-D-11-00009.1.
[12] Mantelli Neto SL, von Wangenheim A, Pereira EB, Comunello E. The Use of Euclidean Geometric Distance on RGB Color Space for the Classification of Sky and Cloud Patterns. Journal of Atmospheric and Oceanic Technology 2010;27:1504–17. doi:10.1175/2010JTECHA1353.1.
[13] Ghonima MS, Urquhart B, Chow CW, Shields JE, Cazorla A, Kleissl J. A method for cloud detection and opacity classification based on ground based sky imagery. Atmospheric Measurement Techniques Discussions 2012;5:4535–69. doi:10.5194/amtd-5-4535-2012.

[14] Linfoot A, Alliss RJ. A cloud detection algorithm applied to a whole sky imager instrument using neural networks. American Meteorological Society, 88th Annual Meeting, Chantilly, Virginia: 2008, p. 1–13.

[15] Li Q, Lu W, Yang J, Wang JZ. Thin Cloud Detection of All-Sky Images Using Markov Random Fields. IEEE Geoscience and Remote Sensing Letters 2012;9:417–21.

[16] Carson C, Belongie S, Greenspan H, Malik J. Blobworld : Image segmentation using Expectation-Maximization and its application to image querying. IEEE Transactions on Pattern Analysis and Machine Intelligence 2002;24:1026–38.

[17] Malik J, Shi J. Normalized cuts and image segmentation. IEEE Transactions on Pattern Analysis and Machine Intelligence 2000;22:888–905. doi:10.1109/34.868688.

[18] Scaramuzza D, Martinelli A, Siegwart R. A Toolbox for Easily Calibrating Omnidirectional Cameras. 2006 IEEE/RSJ International Conference on Intelligent Robots and Systems, Ieee; 2006, p. 5695–701. doi:10.1109/IROS.2006.282372.

[19] Blanc P, Wald L. The SG2 algorithm for a fast and accurate computation of the position of the Sun for multi-decadal time period. Solar Energy 2012;86:3072–83. doi:10.1016/j.solener.2012.07.018.

[20] Ghonima MS, Urquhart B, Chow CW, Shields JE, Cazorla A, Kleissl J. A method for cloud detection and opacity classification based on ground based sky imagery. Atmospheric Measurement Techniques 2012;5:2881–92. doi:10.5194/amt-5-2881-2012.

[21] Yamashita M, Yoshimura M, Iwao K. Monitoring and Discrimination for Sky Conditions using Multi-temporal Whole Sky Imageries. ACRS Proceedings, Hanoi: 2005.

[22] Darula S, Kittler R, Road D. CIE general sky standard defining luminance distributions 1967.

[23] Perez R, Seals R, Michalsky J, Sciences A. All-weather model for sky luminance distribution - preliminary configuration and validation. Solar Energy 1993;50:235–45.

[24] Igawa N, Koga Y, Matsuzawa T, Nakamura H. Models of sky radiance distribution and sky luminance distribution. Solar Energy 2004;77:137–57. doi:10.1016/j.solener.2004.04.016.

[25] Buie D, Monger AG, Dey CJ. Sunshape distributions for terrestrial solar simulations. Solar Energy 2003;74:113–22.

[26] Otsu N. A Threshold Selection Method from Gray-Level Histograms. IEEE Transactions on Systems, Man, and Cybernetics 1979;9:62–6.